MIT Open Access Articles

Experimental Characterization and Modeling of Capillary-Pumped Thin-Film Evaporation From Micropillar Wicks

ICNMM2016-8085

EXPERIMENTAL CHARACTERIZATION AND MODELING OF CAPILLARY-PUMPED THIN-FILM EVAPORATION FROM MICROPILLAR WICKS

Solomon Adera[1], Dion Antao[1], Rishi Raj[2], and Evelyn N. Wang[1],*

[1]Device Research Laboratory
Department of Mechanical Engineering
Massachusetts Institute of Technology
Massachusetts 02139, USA
*Corresponding author: enwang@mit.edu

[2]Thermal and Fluid Transport Laboratory
Department of Mechanical Engineering
Indian Institute of Technology
Patna, Bihar, India 800013

ABSTRACT

Generation of concentrated heat load in confined spaces in integrated circuits and advanced microprocessors has presented a thermal management challenge for the semiconductor industry. Compared to state-of-the-art single phase cooling strategies, phase-change based approaches are promising for cooling the next generation microelectronic devices. In particular, thin-film evaporation from engineered surfaces has received significant attention in the last few decades as a potential candidate since it enables passive transport of the working fluid *via* capillarity in addition to increasing the evaporation area *via* extending the liquid meniscus and three-phase contact line. Thin-film evaporation, however, is coupled with nucleate boiling making experimental characterization as well as modeling of the fluidic and thermal transport a challenging task for thermal engineers. Furthermore, quantifying the relative contributions of nucleate boiling and thin-film evaporation from the experimentally reported heat fluxes has been difficult. Unlike previous studies, our work experimentally characterizes thin-film evaporation in the absence of nucleate boiling from arrays of silicon micropillars. In particular, we characterize the capillary-limit where the microstructured surface dries out due to liquid starvation when the capillary pressure that is generated due to the meniscus shape cannot overcome the viscous losses within the micropillar wick. We modeled the fluidic and thermal transport of the evaporating meniscus by solving the coupled heat and mass transfer equations. Compared to experiments, our model predicts the dryout heat flux with ±20% accuracy. The insights gained from this study provide a suitable platform to design and optimize micropillar wicks for phase-change based thermal management devices such as heat pipes and vapor chambers.

KEY WORDS: phase-change, thin-film evaporation, capillarity, capillary limit, dryout heat flux, micropillar wick, heat pipe

INTRODUCTION

The exponential rise in the number of transistors in a single chip associated with the race to increase functionality and operating speed has continued generating concentrated heat loads in integrated circuits and advanced microprocessors. Currently, this heat load at the device foot print has reached $100\ \text{W/cm}^2$ [1] and it is projected to exceed $300\ \text{W/cm}^2$ in the coming few years [2] creating a thermal management challenge for the microelectronics industry. While enhanced convective single phase cooling solutions have been sufficient in the past, direct extension of the state-of-the-art air cooling technology is inadequate to remove heat loads in excess of $100\ \text{W/cm}^2$ due to the inferior thermophysical properties of air [3, 4]. Furthermore, the improvements that can be achieved *via* convective air cooling is limited (*e.g.*, fan speed). Similarly, single phase liquid cooling requires large pumping power for transporting the working fluid in micro scale devices making it an unfavorable cooling solution for the packaging industry due to low coefficient of performance (COP). As a result, novel thermal management solutions that utilize the latent heat of vaporization as the working fluid changes phase from liquid-to-vapor are sought after to mitigate the current thermal management challenge.

One such candidate is flow boiling in microchannels [5]. However, phase-change microfluidic cooling solutions require significant pumping power in addition to suffering from instabilities that pose a fundamental limit on the thermal performance [6]. Accordingly, inlet restrictors have been used [7] which have led to significant increase in pumping power and negate the advantages of a phase-change approach. An alternative solution that has shown great promise is thin-film evaporation [8-10] from micro/nano-engineered surfaces where capillarity can be utilized to transport the working fluid passively (as opposed to pumping). Furthermore, microstructured surfaces extend the liquid-vapor interface at the three-phase contact line

Copyright © 2016 by ASME

(*i.e.*, the thin-film region) maximizing the phase-change evaporative area.

Our experimental study characterizes thin-film evaporation in the absence of nucleate boiling from a 1×1 cm² microstructured area which is surrounded by a water reservoir. Specifically, we characterized the capillary-limit beyond which the microstructured surface dries out due to insufficient fluidic delivery to compensate for the liquid loss *via* evaporation. The working fluid was transported by creating a pressure gradient (*i.e.*, curvature gradient) along the flow direction (*i.e.*, capillary-wicking). Based on the understanding gained from experiments, we developed a thermal-fluidic model that predicts the capillary-limited dryout heat flux with ±20% accuracy.

NOMENCLATURE
Symbols
A	Area (m²)
D	Diameter (m)
H	Height (m)
h_{fg}	Latent heat of vaporization (J/kg)
I	Current (A)
K	Permeability (m²)
k	Thermal conductivity (W/m·K)
L	Spacing (m)
l	Dryout length (m)
M	Figure of merit (W/m²)
n	Index of refraction (-)
P	Pressure (N/m²)
q''	Heat flux (W/m²)
T	Temperature (K)
ΔT	Superheat (K)
t	Thickness (m)
U	Characteristic velocity (m/s)
u	Velocity (m/s)
$\bar{u}$	Average velocity (m/s)
V	Voltage (v)

Greek
ε	Porosity (-)
θ	Contact angle (°)
μ	Dynamic viscosity (kg/m·s)
ρ	Density (kg/m³)
σ	Surface tension (N/m)
ω	Wave length (m)

Subscripts
cap	capillary
eff	effective
l	liquid
LV	Liquid-vapor
PS	Power source
rec	Receding
sat	Saturation
sub	Substrate

TEST DEVICE DESIGN

The overall dimension of the test device used for this study is 3×3 cm² with the center 1×1 cm² area microstructured for evaporation (Fig. 1a). The microstructured area contains well-defined silicon micropillar arrays in a square pattern (Fig. 1b) which were fabricated *via* photolithography and deep-reactive-ion-etching (DRIE). The diameters (D), heights (H), and center-to-center spacings (L) of the micropillars (Fig. 1b inset) were varied from 8-12, 35-90, and 12-20 μm, respectively for systematic characterization. The D, H, and L used for this study are listed in Table 1. The microstructured area is surrounded by a 6 mm wide primary water reservoir which was created in a one-step DRIE process alongside the micropillars. Consequently, the depth of the water reservoir is the same as the pillar height. The water reservoir was covered from the top by a silicon which was bonded *via* direct fusion bonding. Prior to bonding, four 2.5 mm diameter inlet ports were etched through the top silicon cover *via* DRIE. The working fluid was transported from the primary reservoir to the center of the microstructured surface *via* capillary-wicking (Fig. 1c) [11]. For integrated measurement, a thin-film platinum serpentine heater (H1, Fig. 1d) and three temperature sensors (S1, S2, and S3, Fig. 1d) were patterned on the backside of the test device using electron-beam evaporation and acetone lift-off. A 1 μm thick thermally grown oxide layer was used for dielectrically insulating the heater and sensors from the silicon substrate. After annealing the heater and sensors in a 350 °C nitrogen environment for 4 hrs, the nominal resistances were ≈200 Ω and ≈1200 Ω, respectively. The heater (H1) was designed to provide uniform heating for the 1×1 cm² microstructured area. The sensors (S1, S2, and S3) which are located 3 mm apart along the longitudinal centerline were calibrated to measure the local temperature over a 620×640 μm² area. The calibration was carried out in a convection oven where the temperature was measured using a high accuracy fluid immersion platinum resistance temperature detector (RTD-810, Omega Engineering). The calibration curve (resistance-temperature plot) was highly linear with < 1% root-mean-square-error (RMSE). Besides heating, H1 was calibrated alongside the sensors to measure the average temperature of the entire microstructured/evaporative area (*i.e.*, 1×1 cm²). The sensitivity of the temperature sensors was 2.4 Ω/°C and all temperatures were measured at the backside of the test device.

Table 1: Micropillar dimensions used for this study. The measurement uncertainty for D and H is ±1 μm.

Device ID	D (μm)	H (μm)	L (μm)
1	12	80	20
2	12	90	20
3	12	35	20
4	8	80	12
5	8	82	16
6	8	77	20

Copyright © 2016 by ASME

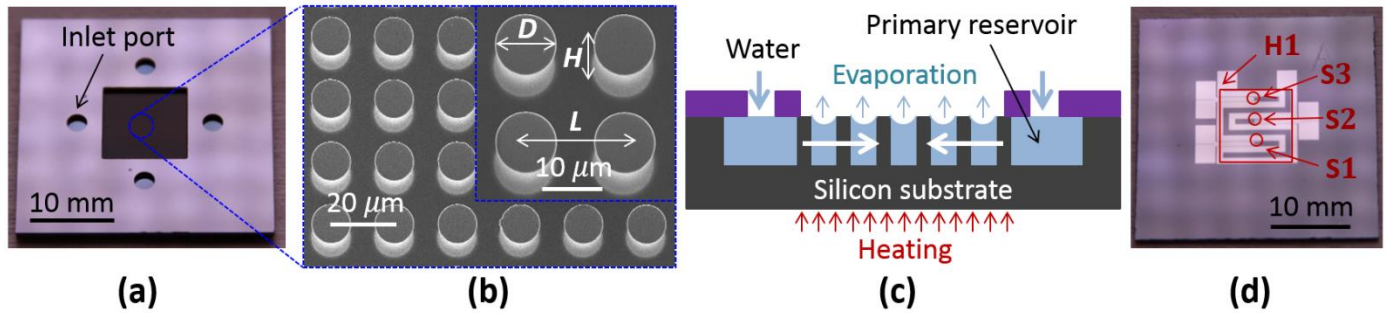**Figure 1:** (a) Test device (3×3 cm^2) with the center 1×1 cm^2 area microstructured. (b) Scanning electron micrograph (SEM) of the microstructured area of device 1 showing pillar diameter (D), height (H), and spacing (L). (c) Schematic of capillarity. Fluidic transport from the primary reservoir to the microstructured surface is due to the variation in the shape of the liquid meniscus from the edge to the center of the microstructured area. (d) Backside of the test device showing the platinum thin-film heater (H1) and sensors (S1, S2, and S3). Besides heating, H1 was used to measure the average backside temperature of the evaporative area, *i.e.*, 1×1 cm^2. The box indicates the evaporative area with respect to the heater location, *i.e.*, the location and size of the heater (H1) on the backside of the test device matches that of the microstructured area on the front. S1, S2, and S3 are 3 mm apart along the centerline and measure the local temperature over a 620×640 μm^2 area.

A device holder which consists of two parts (top cover and bottom fixture) was fabricated from Ultem. The center 1×1 cm^2 of the top cover was cutout (Fig. 2a) to allow unimpeded evaporation. Moreover, a secondary reservoir with an exit port was incorporated in the top cover (Fig. 2a). After filling the primary reservoir, the excess water was flushed out through the exit port without disrupting the liquid transport mechanism within the micropillar wick. Outer and inner silicone gaskets (JTR-S-2.0, Grace Bio-Labs Inc.) were used to avoid lateral flow of the working fluid. Spring-loaded pogo-pins (HPA-1D and SPR-1W, Everett Charles Technologies) were press fit into the bottom fixture (Fig. 2b) for supplying the electrical voltage that was required for heating and temperature sensing *via* electrical wires. The test device was pressed against the pogo-pins and sandwiched between the top cover and bottom fixture in preparation for experiments. The assembly (Fig. 2c) was held together by four threaded bolts.

Chemically inert plastic tubes (polyvinyl chloride) were used to deliver water to the secondary reservoir. The two-reservoir design enabled capillary-wicking where the microstructured surface syphons only the required amount of the working fluid to sustain evaporation, *i.e.*, the liquid meniscus shape adjusts its curvature in response to the heating power. This self-regulating behavior of capillarity decoupled nucleate boiling from thin-film evaporation by suppressing flooding of the microstructured surface and the subsequent boiling. Consequently, all the experimental results reported in this study are pure thin-film evaporation without nucleate boiling.
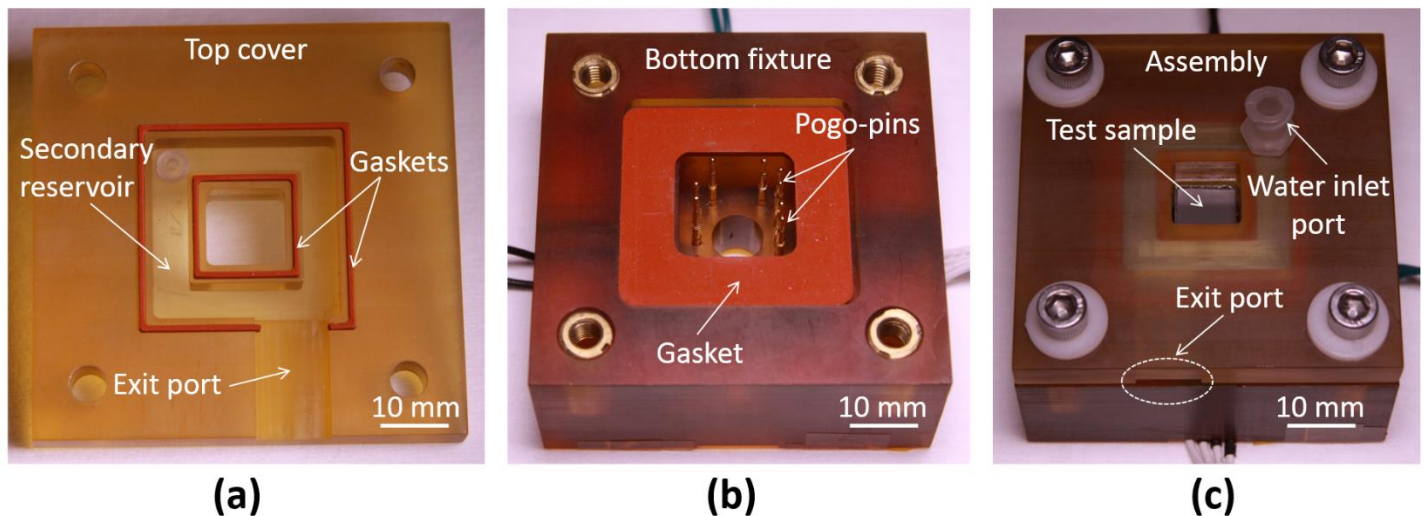

Figure 2: Device holder design. (a) Top cover with integrated secondary reservoir and exit port. After filling the primary reservoir, the excess water leaves the secondary reservoir *via* the exit port. (b) Bottom fixture showing the press fit pogo-pins. The test device was pressed against the spring-loaded pogo-pins for electrical contact. (c) Assembly. The test device was sandwiched between the top cover and bottom fixture by aligning the microstructured surface of the test device with the 1×1 cm^2 cutout section of the top cover.

EPERIMENTAL SETUP

Schematic of the experimental setup is shown in Fig. 3. Test devices were wet cleaned (acetone, methanol, IPA, and de-ionized water), dried with compressed nitrogen, and plasma treated for 30 minutes (PDC-001, Harrick Plasma) in preparation for experiments. The assembly (Fig. 2c) was placed inside a custom built environmental chamber (Kurt J. Lesker Company) and the entire system was evacuated using a vacuum pump (Pascal 2010 SD, Adixen) to remove noncondensable gases. The chamber was then allowed to reach near saturation conditions, *i.e.*, saturation temperature and pressure (≈24 °C and ≈3 kPa). The chamber temperature was measured by inserting calibrated J-type thermocouples *via* a thermocouple feedthrough while the pressure was measured using a Baratron gage capacitance manometer (740C Baratron, MKS Instruments, Inc.,). The heating power to the environmental chamber was controlled using a variable AC power supply. High purity de-ionized (DI) water (Chromasolv for HPLC, Sigma-Aldrich) which was stored outside the chamber in a custom built stainless steel canister was used for all experiments. After degassing the water *via* boiling, it was maintained at saturated conditions (≈60 °C and ≈20 kPa) using a 1/16 DIN ramp/soak PID controller (CN7823, Omega Engineering). The water temperature was measured by inserting a calibrated 12" J-type thermocouple inside the canister (T, Fig. 3). The pressure (P, Fig. 3) which was measured using a

digital pressure gage (DPG5500B, Omega Engineering) matched the NIST-database [12] ensuring the absence of dissolved noncondensable gases in the water supply. The water was transported from the canister to the chamber by utilizing the pressure difference between the canister and chamber (≈17 kPa) to overcome the viscous losses in the valve and piping. The water supply from the canister (≈60 °C) was actively cooled to the chamber temperature (≈24 °C) *via* a water cooled heat exchanger (Lauda RE200, Lauda-Brinkmann). The flow rate was measured using an accurate liquid flow meter (L-50 CCM-D, Alicat Scientific) (V, Fig. 3).

During experiments, the water vapor from evaporation was allowed to condense on the inside walls of the environmental chamber. To avoid gradual increase in the chamber pressure, an additional condensing surface was created by suspending a copper tube inside the environmental chamber. A cold water (≈15 °C) was circulating in the copper tube using a water-to-water heat exchanger (Neslab System-III, Thermo Fisher Scientific). The environmental chamber has visual access and images were captured at 1000 frames per second using a high speed camera (Phantom v7.1, Vision Research). Data was collected using a data acquisition system (cDAQ-9174, National Instruments) which was interfaced to a computer monitor using a custom built LabVIEW script [13].
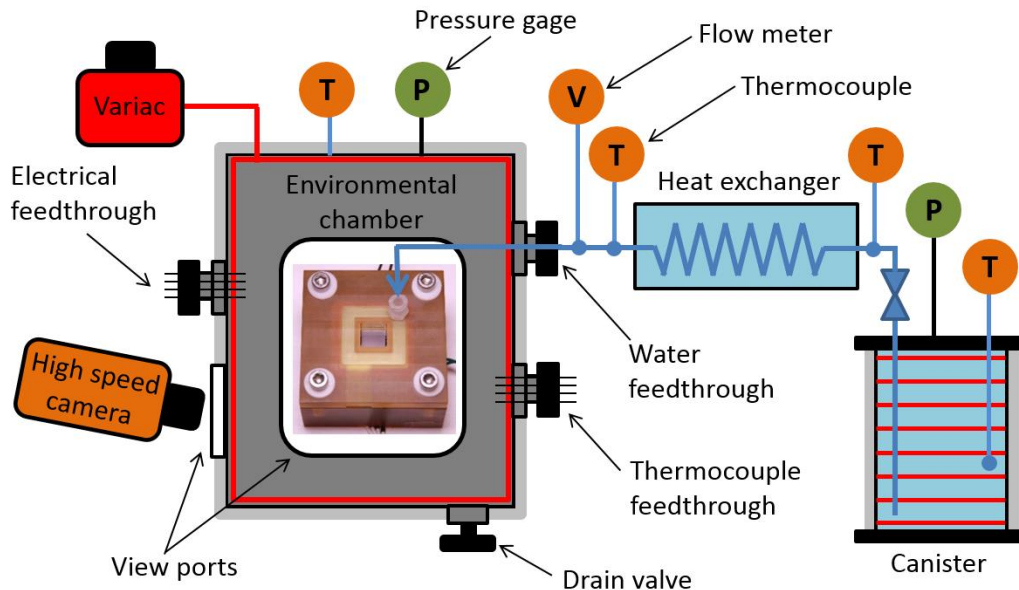

Figure 3: Schematic of the experimental setup with the three main components, *i.e.*, chamber, canister, and heat exchanger. P, T, and V in the schematic stand for thermocouple, pressure gage and liquid flow meter, respectively. Both the chamber and canister were maintained at saturated conditions and all experiments were carried out in the absence of noncondensable gases. The condensate was collected at the end of the experiments *via* a drain valve.

A DC power source (N5752A, Agilent Technologies) was used to heat the test device. The heat flux (q'') was calculated by dividing the heating power by the heated area ($A = 1 \times 1$ cm^2) and it is given by

$$q'' = \frac{V_{PS} I_{PS}}{A}, \qquad (1)$$

where V_{PS} and I_{PS} are the power source voltage and current as measured by a digital multimeter (Keithley 2000, Keithley Instruments), respectively. The temperature which was measured on the backside of our test device was extrapolated to the wall (where the liquid contacts the solid substrate) by assuming a one-dimensional (1D) heat conduction through the silicon

4

Copyright © 2016 by ASME

substrate and the silicon dioxide dielectric insulation layer as given by

$$T_{wall} = T_{back} - q'' \left(\frac{t_{SiO2}}{k_{SiO2}} + \frac{t_{sub}}{k_{sub}} \right), \qquad (2)$$

where T_{wall} and T_{back} are the wall and backside temperatures respectively, t and k are the thickness and thermal conductivity of the respective materials indicated in the subscript (*i.e.*, substrate and silicon dioxide layer), respectively.

RESULTS AND DISCUSSION

We experimentally characterized steady-state pure thin-film evaporation in the absence of nucleate boiling using arrays of micropillars. A typical temporal data for test device 1 with pillar diameter, height, and spacing of 12, 80, and 20, respectively is shown in Fig. 4. During the experiments, the heat flux was increased in a stepwise manner, after maintaining steady-state (± 0.2 °C/min) evaporation for at least 200 s. Similar to the heat flux, the temperature responded in a step-wise manner (Fig. 4a). Due to the high thermal conductivity of silicon and the associated significant heat spreading, the local temperature as measured by the three sensors (S1, S2, and S3) and the average temperature as measured by the heater (H1) were identical (Fig. 4a), suggesting that the entire microstructured surface is nearly isothermal during evaporation. When the capillary pressure fails to overcome the viscous losses within the micropillar wicks, the furthest point from the primary water reservoir (*i.e.*, the center of the microstructured area) dries out due to liquid starvation. The

dry island that forms at the center of the microstructured surface spreads radially outwards causing a temperature spike. Drying out and the subsequent rise in temperature (*i.e.*, thermal runaway) could cause device failure if power was not turned off quickly. The heat flux as a function of superheat (*i.e.*, temperature difference between the wall and the chamber, $\Delta T = T_{wall} - T_{sat}$) is shown in Fig. 4b. The dryout heat flux for device 1 was ≈ 36 W/cm² at ≈ 14 °C superheat as indicated by the last data point in Fig. 4b. For heat fluxes below 36 W/cm², the evaporation was pure thin-film (Fig. 4c). However, at ≈ 36 W/cm², a dry island formed at the center of the microstructured surface (Fig. 4d) and the heat transfer mechanism changed from evaporative to convective cooling. Our experimental results are highly repeatable and independent of the flow rate (Fig. 4e). When the flow rate was increased from 20 to 36 ml/min, both the dryout heat flux and superheat remained within the experimental error (Fig. 4e), confirming the role of capillary-wicking as the sole liquid transport mechanism within the micropillar wick. Unless stated otherwise, the error bars in Fig. 4 and elsewhere in our study were obtained by combining the random and system errors [14]. The system error for temperature measurement was obtained *via* standard error propagation analysis from the measured excitation voltage and current as well as the calibration curve (electrical resistance versus temperature plot). Similarly, the error bar on the heat flux arises mainly from the uncertainty in power source voltage and current measurement.
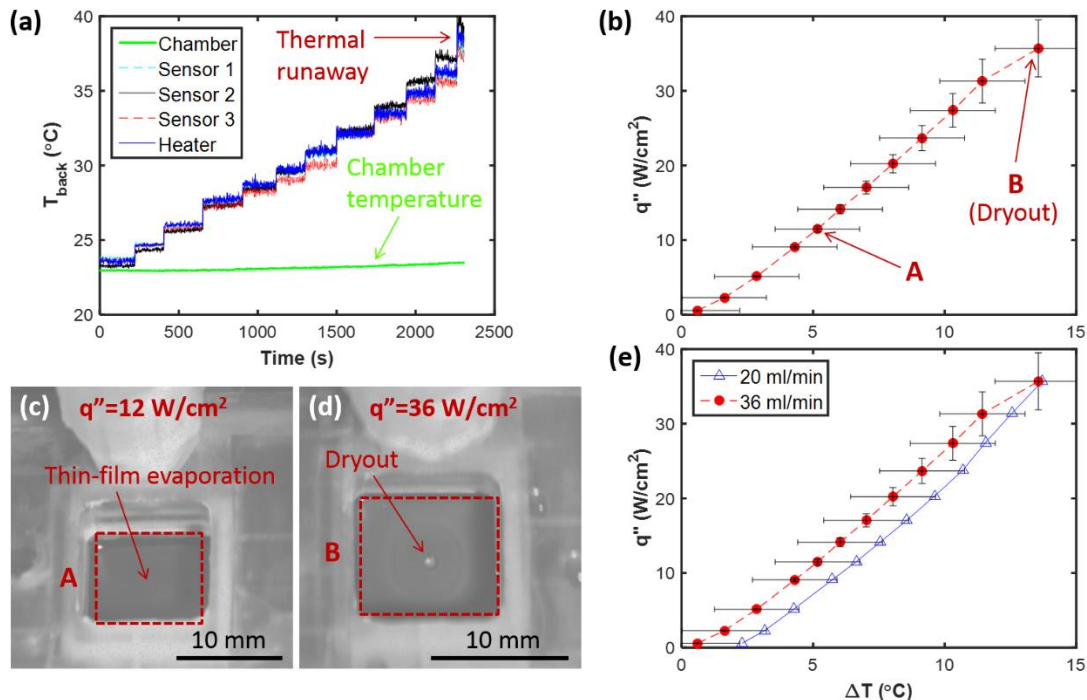

Figure 4: (a) Temporal backside temperature, and (b) heat flux as a function superheat. Optical images of the test device during (c) steady-state pure thin-film evaporation at 12 W/cm², and (d) dryout and thermal runaway at ≈ 36 W/cm². When the viscous losses in the micropillar wick exceeds the pressure difference between the liquid and vapor side of the evaporating meniscus, not enough water is delivered to compensate for the liquid loss *via* evaporation and the center of the microstructured surface forms a dry island. (e) The experimental data is highly repeatable and independent of the flow rate. All the experimental results in the discussion are for device 1.

5

We characterized sensible, convective, and ohmic heat losses in our experiments. The sensible heat loss was estimated by measuring the flow rate and the temperature of the incoming and outgoing water in the secondary reservoir. Similarly, the convective heat loss was estimated conservatively for a $10 \, \text{W/m}^2 \cdot \text{K}$ heat transfer coefficient inside the saturated chamber. Lastly, the ohmic heat loss was calculated by measuring the power source current and the combined resistance in the lead wires, pogo-pins, and electrical feedthrough. We observed that the combined heat loss (*via* sensible, convection, and ohmic) was ≤2% of the input power. This heat loss is deducted from all heat fluxes reported in this study.

MODELING

Fluidic and thermal transport is modeled for the two-dimensional (2D) microstructured surface shown by the schematic in Fig. 5a. We conserved mass, momentum, and energy for the control volume shown by the dotted box in Fig. 5b. Furthermore, we assumed uniform evaporation from the top liquid meniscus. Fluidic transport is driven by the variation in the curvature of the liquid meniscus along the flow direction [11].
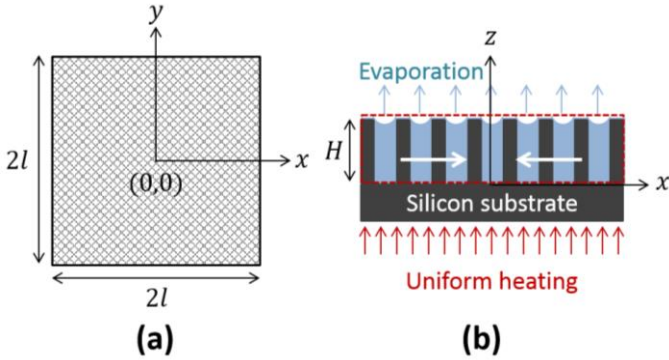

Figure 5: Schematic of the porous domain used for modeling the fluidic and thermal transport as viewed from (a) top (*xy*-plane), and (b) side (*xz*-plane).

Following our assumption that all the heating power was utilized for phase change, the conservation of energy can be written as

$$q'' = \rho_l \bar{u}_z h_{fg}, \tag{3}$$

where ρ_l is the density of the liquid, h_{fg} is the latent heat of vaporization, and $\bar{u}_z$ is the average velocity of the liquid in the *z*-direction. The conservation of mass for incompressible flow ($\nabla \cdot u = 0$) through the porous media is governed by the continuity equation which is given by

$$\frac{\partial \bar{u}_x(x,y)}{\partial x} + \frac{\partial \bar{u}_y(x,y)}{\partial y} + \frac{q''}{H\rho_l h_{fg}} = 0, \tag{4}$$

where $\bar{u}_x$ and $\bar{u}_y$ are the average velocity in the *x*- and *y*-directions, respectively. We assumed laminar (*i.e.*, low Reynolds number) flow in 2D and used the lubrication approximation to simplify the momentum equation for flow in porous media (*i.e*, Brinkman equation) [15, 16]. This is

consistent since the flow of liquid in the direction perpendicular to the surface (H) is much smaller than that occurring in the lateral direction parallel to the surface (l), *i.e.*, $\bar{u}_z \sim \left(\frac{H}{l}\right) U \ll U$ where U is the average characteristic velocity in the lateral (*x* and *y*) direction. The momentum equation for flow in 2D (*x*- and *y*-directions) simplifies to

$$\frac{\partial^2 u_x(x,y,z)}{\partial z^2} = \frac{\varepsilon}{\mu_l} \frac{\partial P(x,y)}{\partial x} + \frac{\varepsilon u_x(x,y,z)}{K},$$

$$\frac{\partial^2 u_y(x,y,z)}{\partial z^2} = \frac{\varepsilon}{\mu_l} \frac{\partial P(x,y)}{\partial y} + \frac{\varepsilon u_y(x,y,z)}{K}, \tag{5}$$

where $P(x,y)$ is the gage pressure, $u_x(x,y,z)$ and $u_y(x,y,z)$ are the *x*- and *y*-direction velocity, respectively, μ_l is the viscosity of the liquid, ε and K are the porosity and permeability of the micropillar wick, respectively. Porosity is defined as the fraction of the total volume of the medium that is occupied by void space. For an isotropic medium, the area fraction of the void is the porosity, *i.e.*, $\varepsilon = 1 - \pi D^2/4L^2$ and $(1 - \varepsilon)$ is the solid fraction. The additional term in the momentum equation (Eq. 5) accounts for the porous nature of the transporting medium which renders additional flow resistance. The boundary conditions for the momentum equation are the no slip boundary condition at the base of the micropillar wick ($z = 0$) and shear free surface at the top liquid-vapor interface ($z = H$) as given by

$$u_x(x,y,z)\big|_{z=0} = 0,$$

$$\frac{\partial u_x(x,y,z)}{\partial z}\bigg|_{z=H} = 0,$$

$$u_y(x,y,z)\big|_{z=0} = 0,$$

$$\frac{\partial u_y(x,y,z)}{\partial z}\bigg|_{z=H} = 0. \tag{6}$$

The expression for the capillary-limited dryout heat flux can be obtained by solving Eqs. 3-5 using the boundary conditions shown in Eq. 6 and noting that the maximum capillary pressure (P_{cap}) is at the center of the microstructured surface, *i.e.*, $P(0,0)$. It is given by

$$q'' = -\frac{HKP_{cap} \frac{\rho_l h_{fg}}{\mu_l}\left(-1 + \frac{\tanh H\beta}{H\beta}\right)}{\frac{l^2}{2} - \frac{2}{l}\sum_{j=1}^{\infty} \frac{\sin(\lambda_j l)}{\lambda_j^3 \cosh(\lambda_j l)}}, \tag{7}$$

where l is the dryout length, $\beta = \sqrt{\varepsilon/K}$, and $\lambda_j = (2j-1)\pi/2l$ for $j = 1,2,3, \dots$ (infinite series). If we use only the first term of the infinite series (*i.e.*, j=1, $\lambda_1 = \pi/2l$), the denominator in Eq. 7 reduces to

$$\frac{l^2}{2} - \frac{2}{l} \frac{\sin(\lambda_1 l)}{\lambda_1^3 \cosh(\lambda_1 l)}\bigg|_{\lambda_1=\pi/2l} \approx 0.3l^2. \tag{8}$$

6

Copyright © 2016 by ASME

The first-term approximation simplifies the expression for the capillary-limited dryout heat flux as

$$q'' \approx \frac{10}{3} \left(\frac{HKP_{cap}}{l^2} \right) \left(1 - \frac{\tanh(H\beta)}{(H\beta)} \right) \left(\frac{\rho_l h_{fg}}{\mu_l} \right). \quad (9)$$

Equation 9 shows that the dryout heat flux is directly proportional to the micropillar wick thickness and permeability, but inversely proportional to the square of the dryout length. Moreover, it is a function of thermophysical properties of the working fluid.

The shape of the liquid meniscus varies from the edge to the center of the microstructured area. An effective micropillar wick thickness (H_{eff}) for fluidic transport is defined by averaging the liquid thickness at the center and edge of the microstructured area. After approximating the liquid meniscus shape as a spherical cap, the effective micropillar wick thickness is given by

$$H_{eff} = H - \frac{(\sqrt{2}L - D)(1 - \sin\theta_{rec})}{4\cos\theta_{rec}}, \quad (10)$$

where θ_{rec} is the receding contact angle (Fig. 6a). Similarly, the permeability is corrected for the meniscus shape (as opposed to a flat meniscus) where the effective permeability (K_{eff}) is given by

$$K_{eff} = K_{2D} \left\{ 1 - \frac{exp(2\beta H_{eff}) - 1}{\beta H_{eff}[exp(2\beta H_{eff}) + 1]} \right\} \Lambda_1 \Lambda_2,$$

$$\quad (11)$$

$$\Lambda_1 = \frac{H_{eff}}{H}, \Lambda_2 = \frac{H_{eff} + \xi}{H + \xi}, \xi = \frac{\varepsilon D}{4(1 - \varepsilon)},$$

where K_{2D} is the permeability from Sangani and Acrivos [17]. The expression in the bracket is a correction factor for the porous nature of the transporting medium (*i.e.*, Brinkman equation) where as Λ_1 and Λ_2 are correction factors for the variation in wetted and cross-sectional areas, respectively [18, 19].

Depending on the heat flux and the evaporation rate, the liquid meniscus dynamically adjusts its curvature to maintain steady-state evaporation. The liquid meniscus at the center of the wick is near flat for low heat fluxes. This curvature increases as the heating power increases. When the contact angle between the liquid-vapor interface and the solid pillar wall reaches the receding contact angle, the liquid meniscus starts to recede and the microstructured area dries out. Before initiation of dryout, the forces due to capillary pressure (*i.e.*, the pressure difference between the vapor and liquid side of the meniscus) and surface tension are in mechanical equilibrium. We estimated the capillary pressure by balancing the pressure and surface tension forces which act on the projected liquid-vapor interface ($L^2 - \pi D^2/4$) and three-phase contact line (πD), respectively (Fig. 6b) as given by

$$P_{cap} = \frac{4\sigma_{LV}\cos\theta_{rec}}{D\left\{ \frac{4}{\pi}\left(\frac{L}{D} \right)^2 - 1 \right\}}, \quad (12)$$

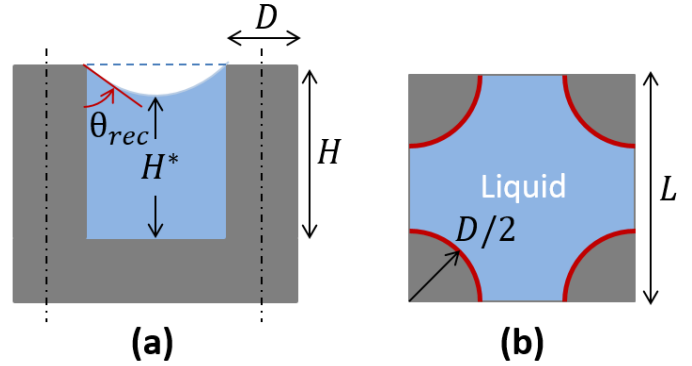where σ_{LV} is the liquid-vapor surface tension.

Figure 6: Unit cell of a square micropillar array viewed from (a) side, and (b) top. The actual micropillar wick thickness (H^*) is smaller than the nominal thickness (H). The solid red quadrants in (b) show the contact line where surface tension forces act.

The receding contact angle was estimated by matching the location of interference fringes which were obtained *via* laser interferometry with Surface Evolver (SE) numerical simulation [20]. The experimental setup for laser interferometry is shown in Fig 7a. When a monochromatic laser beam interacts with a thin liquid film, bright and dark fringes (Fig. 7b) form as a result of interference of the incident and reflected light due to variation in the thickness of the liquid film. The meniscus shape was determined by identifying the in-plane and out-of-plane location of the fringe patterns. The out-of-plane vertical distance which is perpendicular to the receding meniscus (*i.e.*, *z*-direction) between two neighboring fringes (bright and dark pairs) is given by $\omega/4n$ where ω is the wave length of the monochromatic light and n is the index of refraction of water ($n = 1.33$). The in-plane location of the fringes is obtained from knowledge of the pillar spacing and pixel count.

The location of the interference fringes along the *x*-direction (0, a, b, c, and d, Fig. 7b) were compared against the meniscus shapes obtained from SE simulation for different receding contact angles (Fig. 7c). We observed that the location of the fringe patterns match with the meniscus shape obtained from SE for 70° receding contact angle with <1% RMSE. The horizontal error bars in Fig. 7c were obtained from the width of the dark fringes while the vertical error bars were obtained from the out-of-plane height difference between neighboring fringes. The average receding contact angle for all devices used in this study was ≈70±5°. We attribute the high receding contact angle to the presence of a hydrophobic polymer (Octafluorocyclobutane, C_4F_8) on the sidewalls of the pillars which is a residue of the DRIE process. We have verified the presence of carbon (≈11%) and fluorine (≈2%) on the sidewalls of the micropillars *via* X-ray photoelectron spectroscopy (XPS) (Fig. 7d).
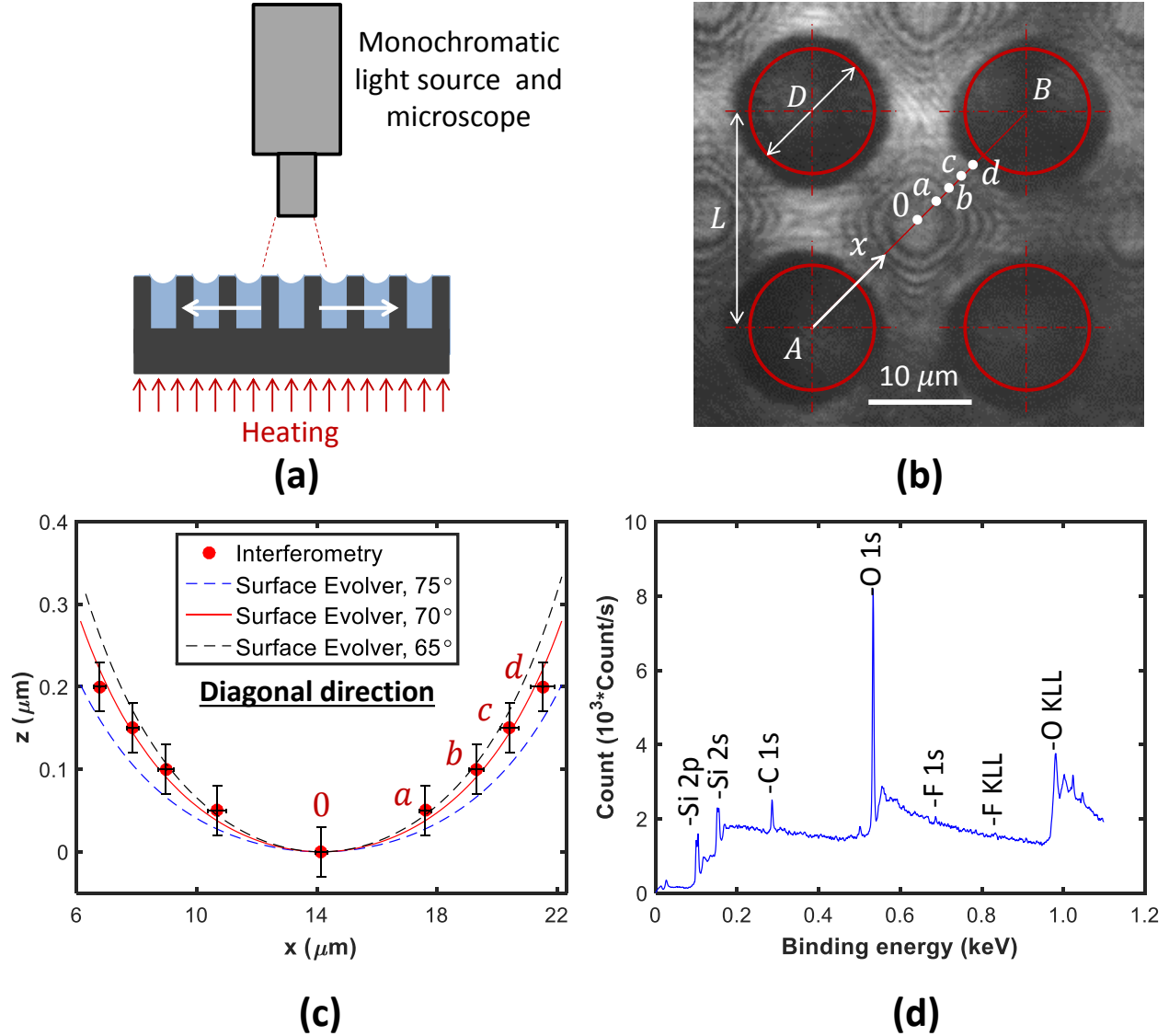
Figure 7: (a) Schematic experimental setup for Interferometry. (b) Interference fringe of a receding meniscus for device 1. Bright and dark fringe patterns form when the incident and reflected lights rays superimpose constructively and destructively, respectively. Due to limitations of the interference technique, points close to the pillars cannot be resolved accurately (*i.e.*, fuzzy fringe pattern). (c) Comparison between SE simulation and interferometry. The side wall of the pillars coincide with the right and left *z*-axis at *x*=6 μm and *x*=22.3 μm. (d) X-ray photoelectron spectroscopy (XPS) of the side walls of the micropillars.

The final expression for the capillary-limited dryout heat flux was obtained from Eq. 9 by substituting for the capillary pressure, corrected micropillar wick thickness and permeability. After rearranging some of the terms, it is given by

$$q'' \approx (40/3)\cos\theta_{rec}\psi^*M,$$

$$\psi^* = \frac{H_{eff}K_{eff}\left\{1 - \frac{\tanh(H_{eff}\beta_{eff})}{(H_{eff}\beta_{eff})}\right\}}{l^2D\left\{\frac{4}{\pi}\left(\frac{L}{D}\right)^2 - 1\right\}}, \tag{13}$$

where $\beta_{eff} = \sqrt{\varepsilon/K_{eff}}$ and M is the figure of merit ($M = \sigma_{LV}\rho_l h_{fg}/\mu_l$) which is a measure of the capillary-limited maximum heat carrying capacity of the working fluid. The figure of merit is a common performance metric and one of the selection criteria for the working fluid in heat pipe technology [21, 22]. For DI water at 24 °C saturation temperature, $M \approx 1.9 \times 10^{11}$ W/m². The effect of the micropillar dimensions on the dryout heat flux is lumped into the dimensionless parameter ψ^*. Equation 13 can be easily adopted to other working fluids. Furthermore, it provides useful insight that can be used to improve the design of porous microstructures for phase-change based thermal management devices.

8

Copyright © 2016 by ASME

MODEL VALIDATION

To characterize the effect of micropillar wick thickness on the dryout heat flux, we carried out experiments on three samples (samples 1-3) which has the same D ($\approx$12 μm) and L ($\approx$20 μm) but different H ($\approx$35-90 μm). The dryout heat flux increases as H increases from 35 to 90 μm (Fig. 8a). Both the experiment and model show that the dryout heat flux scales linearly with the micropillar wick thickness, i.e., $q''\sim H$ (Fig. 8b). Similarly, we characterized the effect of spacing on the dryout heat flux by using three samples (samples 4-6) which has similar D ($\approx$8 μm)

and H ($\approx$77-82 μm) but different L (12, 16, and 20 μm). For constant D and H, when L increases from 12 to 20 μm, the gain in permeability exceeds the loss in capillarity resulting in a net increase in the dryout heat flux (Fig. 8c). This trend is expected to reach an optimum spacing beyond which the gain in permeability cannot compensate for the loss in capillarity resulting in a decrease in heat flux. Our model shows that this optimum spacing is $\approx$50 μm (Fig. 8d). The dotted lines in Fig. 8b and Fig 8d are model prediction (i.e., Eq. 13).
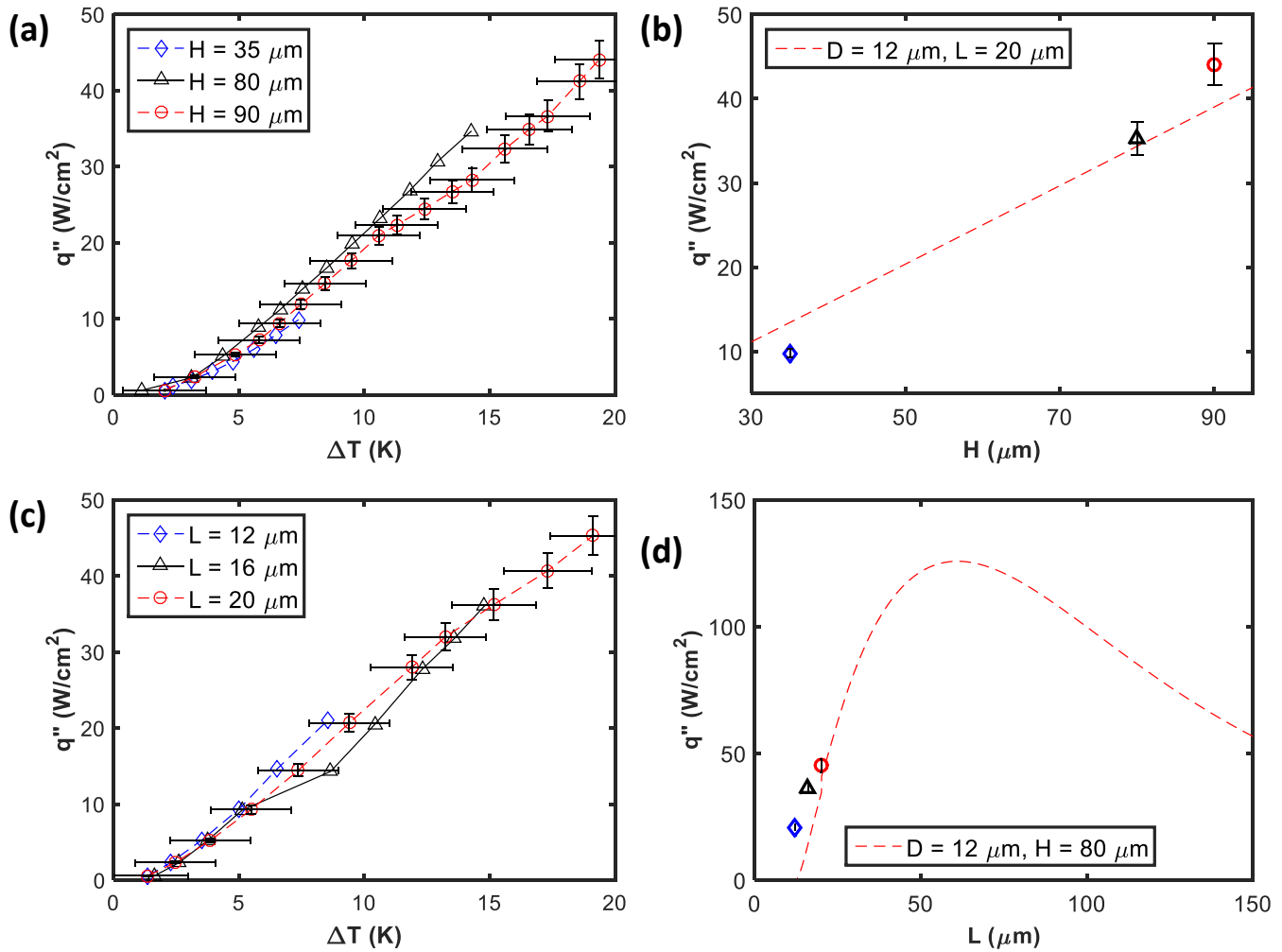

Figure 8: Effect of micropillar wick thickness on the dryout heat flux (a-b). Both the model and experiment show that the capillary-limited dryout heat flux scales linearly with micropillar wick thickness. Effect of spacing on the dryout heat flux (c-d). The model shows that there is an optimum spacing that maximizes the fluidic and thermal transport.

We validated our model by comparing the model prediction (Eq. 13) against the experimentally measured heat flux (Eq. 1) for various samples with varying micropillar dimensions. Our model prediction agrees reasonably well with the experimental data within ±20% accuracy (Fig. 9). We attribute the discrepancy between model prediction and experimental data to non-isothermal liquid meniscus and non-uniform evaporation. Unlike our assumption, the entire liquid-vapor interface is not at

a uniform temperature, i.e., the meniscus near the pillars is at a higher temperature than the meniscus far from the pillars. This will cause a non-uniform evaporation which is not captured in our model. Lastly, the temperature of the saturated chamber and the liquid-vapor interface are not identical unlike our assumption. However, measuring the temperature of the evaporating meniscus is beyond the scope of this study as it requires high spatial and temporal resolution measurement tools.
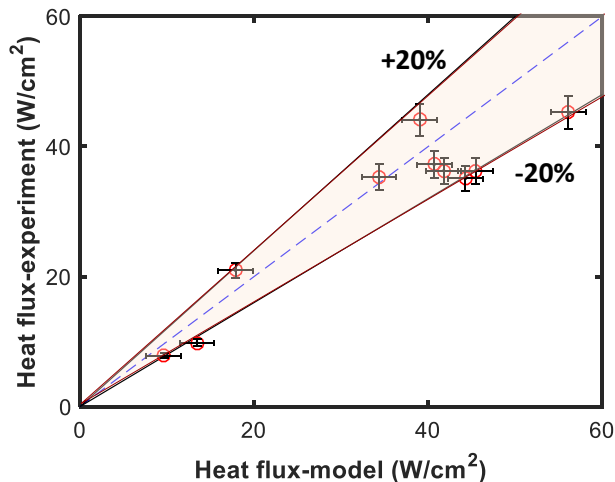
Copyright © 2016 by ASME

Figure 9: Model validation. The model prediction for the dryout heat flux agrees reasonable well with the experiment. The blue dashed line is a 45° line for easy comparison between experiment and model.

CONCLUSIONS

This study characterizes capillary-limited thin-film evaporation in the absence of nucleate boiling. We dissipated ≈36 W/cm² at ≈14 °C superheat from a 1×1 cm² microstructured area. The experimental results are highly repeatable and independent of flow rate. The microstructured area dries out due to liquid starvation when the viscous losses exceed the capillary pressure. Dryout commences at the furthest point from the water reservoir (*i.e.*, center of the microstructured area) and grows radially outwards. It is manifested by a sudden temperature spike which can damage the device (*i.e.*, thermal runaway).

We developed a thermal-fluidic model by simultaneously solving the mass, momentum and energy equations. Our model predicts the dryout heat flux for capillary pumped thin-film evaporation from microstructured surfaces. The model prediction for the dryout heat flux agrees with the experimental data within ±20% accuracy. Both the model and experiment show that the dryout heat flux scales linearly with micropillar wick thickness. Furthermore, the model shows that there is an optimum pillar spacing that optimizes fluidic and thermal transport. More importantly, the model can be adopted for different working fluids and various porous media. The insights gained from this study can be used to improve the design of wicking structures in heat pipes and vapor chamber technology.

ACKNOWLEDGMENTS

REFERENCES

[1] E. Pop, *et al.*, "Heat generation and transport in nanometer-scale transistors," in *Proc. IEEE*, 2006, pp. 1587-1601.

[2] J. R. Thome, "The new frontier in heat transfer: microscale and nanoscale technologies," *Heat Transfer Eng.,* vol. 27, pp. 1-3, 2006.

[3] R. Mahajan, *et al.*, "Cooling a microprocessor chip," in *Proc. IEEE*, 2006, pp. 1476-1486.

[4] I. Mudawar, "Assessment of high-heat-flux thermal management schemes," *IEEE Trans. Compon. Pack. Tech.,* vol. 24, pp. 122-141, 2001.

[5] P.-S. Lee and S. V. Garimella, "Saturated flow boiling heat transfer and pressure drop in silicon microchannel arrays," *Int. J. Heat Mass Transfer,* vol. 51, pp. 789-806, 2008.

[6] S. G. Kandlikar, "Fundamental issues related to flow boiling in minichannels and microchannels," *Exp. Therm. Fluid Sci.,* vol. 26, pp. 389-407, 2002.

[7] A. Koşar, *et al.*, "Suppression of boiling flow oscillations in parallel microchannels by inlet restrictors," *J. Heat Transfer,* vol. 128, pp. 251-260, 2006.

[8] B. Deryagin, *et al.*, "To the theory of liquid evaporation from capillaries," *Kolloidn. Zh.,* vol. 26, pp. 301-307, 1964.

[9] P. Wayner and C. Coccio, "Heat and mass transfer in the vicinity of the triple interline of a meniscus," *AIChE J.,* vol. 17, pp. 569-574, 1971.

[10] V. P. Carey, *Liquid-vapor phase-change phenomena: an introduction to the thermophysics of vaporization and condensation processes in heat transfer equipment*. New York: Hemisphere, 1992.

[11] Y. Wang and G. Peterson, "Analytical model for capillary evaporation limitation in thin porous layers," *J. Thermophys. Heat Transfer,* vol. 17, pp. 145-149, 2003.

[12] F. D. Rossini, *et al.*, *Selected values of chemical thermodynamic properties* vol. 500: US Government Printing Office Washington, DC, 1952.

[13] L. U. Manual, "National Instruments," *Austin, TX,* 1998.

[14] S. G. Rabinovich, *Measurement errors and uncertainties: theory and practice*, Third ed. New York: Springer, 2006.

[15] H. Brinkman, "A calculation of the viscous force exerted by a flowing fluid on a dense swarm of particles," *Appl. Sci. Res.,* vol. 1, pp. 27-34, 1949.

[16] D. A. Nield and A. Bejan, *Convection in porous media*, Fourth ed. New York: Springer, 2013.

[17] A. Sangani and A. Acrivos, "Slow flow past periodic arrays of cylinders with application to heat transfer," *Int. J. Multiphase Flow,* vol. 8, pp. 193-206, 1982.

[18] C. Byon and S. J. Kim, "The effect of meniscus on the permeability of micro-post arrays," *J. Micromech. Microeng.,* vol. 21, pp. 115011-7, 2011.

[19] S. Ravi, *et al.*, "A novel method for characterization of liquid transport through micro-wicking arrays," *Microfluid. Nanofluid.,* vol. 17, pp. 349-357, 2014.

[20] K. A. Brakke, "The surface evolver," *Exp. Math.,* vol. 1, pp. 141-165, 1992.

[21] R. McGlen, *et al.*, *Heat pipes: theory, design and applications*, Fifth ed. Burlington: Elsevier, 2006.

[22] G. P. Peterson, *An introduction to heat pipes : modeling, testing, and applications*. New York: Wiley, 1994.